APL Materials

RESEARCH ARTICLE | JUNE 12 2023

Structural modulation and spin glassiness upon oxidation in oxygen storage material *Ln*FeMnO$_{4+x}$ for *Ln* = Y, Lu, and Yb

Special Collection: Challenges and Perspectives in Materials Chemistry—A Celebration of Prof. Sir Anthony K. Cheetham's 75th Birthday

Tianyu Li ; Sz-Chian Liou; Stephanie J. Hong; Qiang Zhang ; H. Cein Mandujano ; Efrain E. Rodriguez

APL Mater. 11, 061120 (2023)
https://doi.org/10.1063/5.0144717
CHORUS

Structural modulation and spin glassiness upon oxidation in oxygen storage material $LnFeMnO_{4+x}$ for Ln = Y, Lu, and Yb

Cite as: APL Mater. 11, 061120 (2023); doi: 10.1063/5.0144717
Submitted: 31 January 2023 • Accepted: 29 May 2023 •
Published Online: 12 June 2023

Tianyu Li,[1] Sz-Chian Liou,[2] Stephanie J. Hong,[1] Qiang Zhang,[3] H. Cein Mandujano,[1] and Efrain E. Rodriguez[1,a)]

AFFILIATIONS

[1] Department of Chemistry and Biochemistry, University of Maryland, College Park, Maryland 20742, USA
[2] Advanced Imaging and Microscopy Laboratory, Maryland NanoCenter, University of Maryland, College Park, Maryland 20742, USA
[3] Neutron Scattering Division, Oak Ridge National Laboratory, Oak Ridge, Tennessee 37831, USA

Note: This paper is part of the Special Topic on Challenges and Perspectives in Materials Chemistry—A Celebration of Prof. Sir Anthony K. Cheetham's 75th Birthday.
[a)] **Author to whom correspondence should be addressed:** efrain@umd.edu

ABSTRACT

The mixed valence multiferroic $LnFe^{2+}Fe^{3+}O_4$ (where Ln = Y, Lu, and Yb) can reversibly uptake oxygen into its lattice, which is evidenced by a crystallographic phase transition along with the appearance of structural modulations. In this study, we show that the Mn-substituted version of this multiferroic can also be readily oxidized to $LnFe^{3+}Mn^{3+}O_{4.5}$ revealing similar oxygen storage behavior. Through neutron, electron, and synchrotron x-ray diffraction studies, we observe a structural modulation that we attribute to a displacement wave in the fully oxidized compound. This wave exhibits commensurability with a wavevector $\boldsymbol{q}$ = (−2/7, 1/7, 0). Bond valence summation analysis of plausible interstitial oxygen positions suggests that oxygen insertion likely occurs at the middle of the Fe/Mn–O bipyramid layers. The structural modulation of $LnFeMnO_{4.5}$ is two-dimensional, propagates along the *ab*-plane, and is highly symmetric as 12 identical modulation vectors are observed in the diffraction patterns. The nature of the lanthanide, Ln^{3+}, does not seem to influence such modulations since we observe identical satellite reflections for all three samples of Ln = Y, Lu, and Yb. Both $LnFeMnO_4$ and $LnFeMnO_{4.5}$ display spin glassy behavior with 2D short-range magnetic ordering being observed in $LnFeMnO_4$. Analysis of the neutron diffraction data reveals a correlation length of ~10 nm. Upon oxidation to $LnFeMnO_{4.5}$, the short-range magnetic order is significantly suppressed.

I. INTRODUCTION

Hexagonal-layered $LnM^{2+}M^{3+}O_4$ (Ln = lanthanide, *M* = transitional metal) has been attracting great interest in materials chemistry and physics due to its unique crystal structure and high tunability in compositions.[1–4] The structure of $LnM^{2+}M^{3+}O_4$ consists of alternating layers of edge-sharing LnO octahedra with a double layer of edge-sharing MO trigonal bipyramids. The M^{2+} and M^{3+} cations occupy the same crystallographic sites. In the LnO octahedra layer, the Ln^{3+} cations arrange in a triangular lattice, whereas in the MO layer, the M^{2+}/M^{3+} cations are found in a non-corrugated honeycomb lattice. Both the triangular[5] and the honeycomb[6] lattices can display geometric frustration relevant to magnetism. This potential spin frustration has attracted attention from the condensed matter community as this family of oxides could host quantum spin-liquid behavior. Such candidates include those where S = 1/2 as found in $YbMgGaO_4$,[7–10] $YbZnGaO_4$,[11,12] and $LuCuGaO_4$.[13] The fact that M^{2+} and M^{3+} share the same crystallographic site also leads to a great variety of interesting chemical and physical phenomena. In the famous case of mixed-valence $LnFe_2O_4$, where Fe^{2+} and Fe^{3+} coexist at the same sites, ferrimagnetic ordering coincides with charge ordering between Fe^{2+} and Fe^{3+}, leading to multiferroicity.[14–19]

Oxygen non-stoichiometry in $LnM^{2+}M^{3+}O_4$ has also attracted great interest since physical properties of $LnM^{2+}M^{3+}O_4$, especially $LnFe_2O_4$, are extremely sensitive to oxygen stoichiometry.[20–25] However, the oxygen-abundant form of $LnFe_2O_{4+\delta}$ was not realized until Hervieu *et al.* observed that $LuFe_2O_4$ could be oxidized to the hyper-stoichiometric $LuFe_2O_{4.5}$ at a relatively low temperature of 200 °C in air.[26] The oxygen uptake behavior of other $LnFe_2O_4$ (Ln = Yb, Y, and In) was later reported following this discovery.[27–31] The structural transition from $LnFe_2O_4$ to $LnFe_2O_{4.5}$ is also found to be highly reversible, implying a reversible oxygen uptake/release behavior in the $LnFe_2O_4$ system.[29,30,32] The oxygen uptake behavior of $LnFe_2O_4$ suggests its potential as an oxygen storage material and can also lead to interesting structure transitions and physical property changes.[26,29]

Inspired by the interesting oxygen uptake behavior in $LnFe_2O_4$, we hypothesize that the substitution of Fe^{2+} by Mn^{2+} will control the oxygen uptake behavior and the nature of associated structural transitions and magnetism. In this study, we systematically explore the change before and after the oxidation of $LnFe^{3+}Mn^{2+}O_4$. We focus on the difference in the average structure, local structure, structural modulation, and magnetic properties between the reduced phase and corresponding oxidized phase. We investigate the possible influence of the Ln cations on oxygen uptake and compare them with their $LnFe_2O_4$ analogs.

II. EXPERIMENT

A. Materials synthesis

$LnMnFe_2O_4$ (Ln = Yb, Lu, and Y) series, labeled as the reduced phases, were prepared using solid-state reactions.[2] Ln_2O_3 (Ln = Yb, Lu, and Y), Fe_2O_3, MnO, and Fe powder (99.9% pure) were ground in a 1:1:2 ratio, respectively, to prepare around 2 g of the target compound. The powder mixtures were pressed into pellets of 13 mm in diameter. The pellets were placed in a 2 ml alumina crucible and sealed inside evacuated 8 mm diameter quartz ampoules. The ampoules were then heated to 1180 °C (heating rate 10 °C/min) for at least 12 h and subsequently quenched in an ice water bath.

The AB_2O_4 phase is metastable; hence, quenching is required to kinetically lock it in at lower temperatures. Quenching limits the number of oxide impurities. The elemental ratio of the product was verified with ICP and scanning electron microscopy (SEM, Hitachi SU-70) in conjunction with energy dispersive spectroscopy (EDS, Bruker XFlash 6/60), SEM-EDS. To prepare the oxidized phases, $LnMnFe_2O_{4.5}$ (Ln = Yb, Lu, and Y), for *ex situ* studies, the as-synthesized samples were oxidized at 600 °C (heating rate 10 °C/min) under air for 12 h and then cooled to room temperature. These samples are labeled as oxidized phases.

B. Thermogravimetric analysis (TGA)

TGA was conducted on reduced phase $LnMnFe_2O_4$ (Ln = Yb, Lu, Y). In total, 5–10 mg of sample was used for each measurement. TGA measurement with isotherm heating was performed. Samples of ~10 mg were heated to 350 °C (ramping rate 10 °C/min) in air, and the temperature was held for 6 h.

C. High-resolution synchrotron x-ray and neutron diffraction

$LnMnFe_2O_4$ (Ln = Yb, Lu, and Y) series as well as their oxidized phases $LnMnFe_2O_{4.5}$ were characterized with high-resolution synchrotron x-ray powder diffraction (SXPD). The experiments were performed on the 11-BM beamline at the Advanced Photon Source (APS) at Argonne National Laboratory. X-rays were of wavelength 0.457 895 Å. Room temperature data were collected. To compare with the SXPD patterns and explore the possible magnetic structures, we also took time-of-flight (TOF) neutron diffraction patterns for $LnMnFe_2O_4$ and $LnMnFe_2O_{4.5}$ at different temperatures between 5 and 300 K. The TOF patterns were collected on the powder diffractometer POWGEN beamline at the Spallation Neutron Source (Oak Ridge National Laboratory). Rietveld analysis was carried out using JANA[33,34] and GSASii.[35] Structures of oxidized phases were solved using the charge flipping method.[36,37] Structural modulation of the oxidized phase was refined with JANA.

D. Synchrotron x-ray and neutron pair distribution function analysis

The x-ray total scattering data used for x-ray (λ = 0.457 895 Å) pair distribution function (XPDF) analysis were collected on the 11-IDB beamline also at the APS. Data were collected at room temperature (~300 K) and were reduced using GSASii.[35] Neutron total scattering data were obtained at the POWGEN beamline at the SNS. Data were collected at 5 and 300 K.

E. Raman spectroscopy

Raman spectroscopy was obtained with Yvon Jobin LabRam ARAMIS using a 532 nm laser source. Powders were used for the measurement. Because the samples strongly absorb the laser light and can be oxidized, a long exposure time (>5 min) and a small aperture were used to obtain the Raman scattering signal.

F. Transmission electron microscopy (TEM) and electron energy loss spectroscopy (EELS)

Transmission electron microscopy (TEM) images, as well as electron diffraction patterns, were taken using a JEOL 2100F field emission gun (scanning) TEM, (S)TEM, equipped with Gatan image filter (GIF, model of Tridiem 863), operated at 200 kV accelerating voltage.

G. Magnetic susceptibility measurement

Temperature-dependent magnetic susceptibility measurements were performed on both reduced and oxidized phases with a SQUID magnetic property measurement system (MPMS, Quantum Design). For each sample, a portion of powder with known mass was loaded into a gel capsule with cotton suspended inside a plastic straw. Field-cooled (FC) and zero field-cooled (ZFC) magnetization measurements were recorded in direct current mode from room temperature (300 K) to base temperature under an applied field of 100 Oe. Zero field AC susceptibility at 1, 10, 100, and 1000 Hz was also performed at the temperature range of interest.

III. RESULTS

A. Average structure

Since crystal structure of $LnMnFeO_4$ (Ln = Lu, Yb, and Y) is isostructural to the parent phase $LnFe_2O_4$ (space group $R\bar{3}m$),[2,4,38] we used the latter's structure as the starting model for our Rietveld analysis. The refinements were performed with combined neutron and synchrotron x-ray powder datasets. The neutron diffraction pattern with the Rietveld refinement fit for the $YbFeMnO_4$ sample is displayed in Fig. 1(a), and the corresponding plots for the Ln = Lu and Y samples are presented in Figs. S4 and S8. The refined lattice parameters and atom positions of $LnMnFeO_4$ (Ln = Lu, Yb, and Y) are shown in Tables S1, S3, and S6.

No significant difference was found between $LnMnFeO_4$ and $LnFe_2O_4$. The Ln site displays significant displacement along the c-direction, which is commonly observed in the $LnM^{2+}M^{3+}O_4$ phase.[29,39] We noted that some studies use a structure model, where the position of Ln (0, 0, and 0) is split into two partially occupied sites (0, 0, and 0 ± δ).[40] Both models suggest a static positional disorder on the Ln site.

We performed TGA measurement on $LnMnFeO_4$ under the oxygen flow, and the result for $YbFeMnO_4$ is displayed in Fig. 2 (Ln = Lu, Y in Figs. S4b and S8b). Similar to what was observed for $LnFe_2O_4$ (Ln = Lu, Yb, and Y),[26,29,30,32] $LnFeMnO_4$ also uptakes oxygen into its lattice at a relatively low temperature of 200 °C. The maximum weight gain was 2.51%, 2.21%, and 3.88%, corresponding to the change from $LnFeMnO_4$ to $LnFeMnO_{4.5}$. Assuming that Mn^{2+} is oxidized to Mn^{3+}, the theoretical mass gain should be 2.29, 2.3, and 3.03% for Ln = Lu, Yb, and Y, respectively.

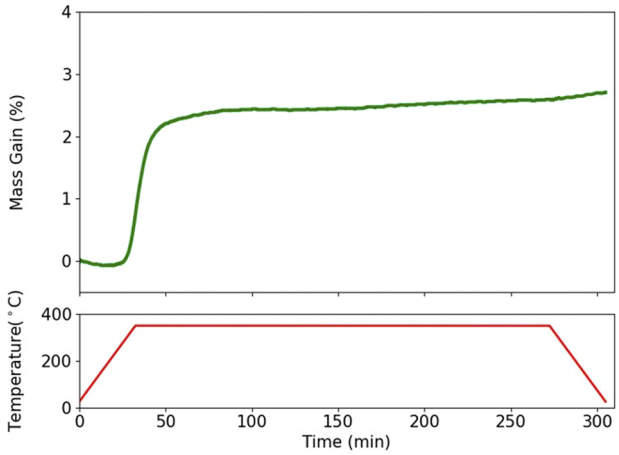

FIG. 2. Mass gaining of $YbFeMnO_4$ heating under air.

To verify the Mn oxidation state, we took electron energy-loss (EEL) spectra of Mn before and after oxidation (Fig. S13). By examining the electron energy-loss near-edge structure (ELNES) on the Mn $L_{2,3}$-edge, which corresponds to the transitions from the Mn $2p$ core orbitals to the unoccupied Mn $3d$ state (dipole selection rule $\Delta\ell = \pm 1$, where ℓ is an angular quantum number),[41] one can obtain information on the chemical coordination of Mn. Our EELS results confirm that the Mn valence state transits from Mn^{2+} into

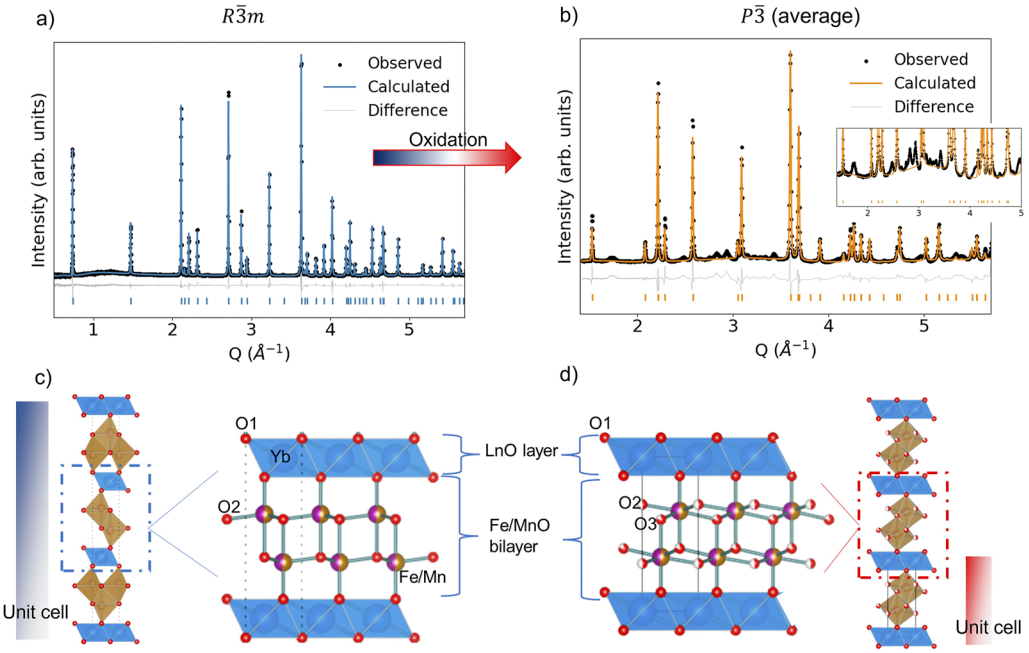

FIG. 1. (a) Neutron powder diffraction pattern and the Rietveld refinement fit of (a) reduced phase $YbMnFeO_4$ and (b) oxidized phase $YbMnFeO_{4.5}$. Crystal structure of (c) $YbMnFeO_4$ and (e) average crystal structure of $YbMnFeO_{4.5}$ (Both $P\bar{3}$ and $P\bar{3}m1$ lead to the identical structure.).

Mn^{3+},[42] and more details on the ELNES analysis can be found in the supplementary material.

The powder diffraction patterns of $LnFeMnO_{4.5}$ can be indexed with the $P\bar{3}$ space group, the same that was found in $YbFe_2O_{4.5}$[29] and $LuFe_2O_{4.5}$.[26] However, we also found space group $P\bar{3}m1$ to provide an identical fit. We then, therefore, applied the charge flipping method to the SXRD patterns to elucidate the crystal structure of the oxidized phase, $LnFeMnO_{4.5}$. Such a methodology helped determine the details of the Ln (Ln = Yb, Lu, and Yb), Fe/Mn, and one of the oxygen atom positions(O1). Afterward, we employed a Fourier difference map to locate the average positions of other oxygen atoms (O2 and O3) with both the NPD and SXRD datasets. Combined refinement was then performed based on the solved structure.

The neutron diffraction pattern with the Rietveld refinement fit of $LnFeMnO_{4.5}$ is shown in Fig. 1(b) for Ln = Yb and Figs. S4c and S8c for Ln = Lu and Y. The refined lattice parameters and atom positions for $LuFeMnO_{4.5}$, $YbFeMnO_{4.5}$, and $YFeMnO_{4.5}$ are included in Tables S2, S4, and S6. Not surprisingly, the solved average structure of $LnFeMnO_{4.5}$ (Ln = Lu, Yb, and Y) resembles what is reported on $YbFe_2O_{4.5}$[29] and is highly correlated with the original reduced phase $LnFeMnO_4$. Figures 1(c) and 1(d) show the structure of $LnMnFeO_4$ and $LnFeMnO_{4.5}$, respectively. Both $P\bar{3}$ and $P\bar{3}m1$ space groups can lead to the same structure for $LnFeMnO_{4.5}$ because the atoms only occupy special locations.

From $LnMnFeO_4$ to $LnFeMnO_{4.5}$, the abundant oxygen atoms are inserted in the middle of Fe/Mn oxide bipyramid double layers, which leads to the shift of the layers along the *ab*-directions.[29] Due to the layer shift, the newly generated unit cell is only 1/3 of the original unit cell ($a_o = a_r$, $c_o = 1/3c_r$). Among all three $LnFeMnO_{4.5}$ (Ln = Lu, Yb, and Y) samples, we noted that the diffraction peaks for $LnFeMnO_{4.5}$ show a broader and more asymmetric nature than $LnFeMnO_4$, which is an indication of stacking faults upon oxidation.[43,44] The appearance of the stacking faults also implies the layer-shift mechanism upon oxygen uptake.

We note that the refinement on the $LnFeMnO_{4.5}$ with the solved average structure gives relatively high R_{wp} values (16%). The misfit mainly arises from the unaccounted satellite peaks [Figs. 1(b), S4c, and S8c], which are similar in all three samples of Ln. The appearance of the satellite peaks indicates a structural modulation,[45,46] which has also been observed in $YbFe_2O_{4.5}$[29] and $LuFe_2O_{4.5}$.[26] Given the similarity of the average structures between $LuFe_2O_{4.5}$/$YbFe_2O_{4.5}$, structural modulation in $LnFeMnO_{4.5}$ is expected. However, the positions and the distributions of the satellite peaks in $LnFeMnO_{4.5}$ (Ln = Lu, Yb, and Y) appear to be completely different from those reported in $YbFe_2O_{4.5}$ and $LuFe_2O_{4.5}$. We will discuss the structural modulation of $LnFeMnO_{4.5}$ in detail in Sec. III C. For both $LnMnFeO_4$ and $LnMnFeO_{4.5}$ (Ln = Lu, Yb, and Y), no cation ordering was observed for the Mn and Fe positions.

B. Local structure

The Rietveld refinement results indicate that the oxidation of $LnFeMnO_4$ to $LnFeMnO_{4.5}$ leads to a considerable contraction in the *c*-direction and a slight expansion along the *a*-direction when the unit cells are normalized to the same chemical formula ($a_r = 1/3c_r$, $a_o = c_o$). This trend is not influenced by the nature of Ln, as shown in Tables S1–S6. This *c*-direction contraction is also evidenced by the

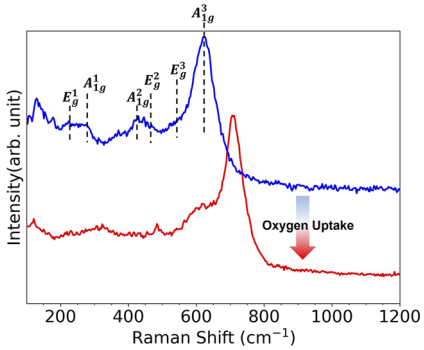

FIG. 3. Raman spectroscopy comparison between $YbMnFeO_4$ and its oxidized phase $YbMnFeO_{4.5}$.

Raman measurements (Figs. 3, S4g, and S7g), which afford information on the local structure. The Raman spectrum of $LnFe_2O_4$ is well studied,[47–52] and the spectrum we recorded of $YbFeMnO_4$ (blue curve in Fig. 3) resembles that of $LnFe_2O_4$. The major phonon modes of $YbFeMnO_4$ are assigned based on the Raman spectra studies of $LnFe_2O_4$.[51]

For the Raman spectra of the oxidized phase $YbFeMnO_{4.5}$ (red curve), we were not able to assign the phonon modes exactly due to the new space group symmetry and structural modulations. However, the structures of $YbFeMnO_4$ and $YbFeMnO_{4.5}$ are highly correlated; hence, there must be some resemblance between their phonon modes. The most intense peak (assigned to A^3_{1g} at 610 cm^{-1}) for the reduced phase $YbFeMnO_4$ corresponds to the stretching vibration of the lattice along the *c*-direction. After oxidation to $YbFeMnO_{4.5}$, the layered framework remains; thus, this A^3_{1g} mode should still exist in the oxidized phase. We argue that the most intense peak blueshifts to 720 cm^{-1} for $YbFeMnO_{4.5}$. Based on such an assignment, oxidation of these materials leads to stronger covalency and shorter bond distances along the c-direction.

Neutron PDF analysis also affords information on the local structure. The PDF curves before and after oxidation are presented in Fig. 4 for Ln = Yb (Fig. S4f for Ln = Lu). The comparison of neutron PDFs indicates that oxidation mainly changes the local environment of the Fe/Mn and O atoms. The Fe–O1 distance (along the *c*-direction) is shortened, and the Fe–O2 distance is elongated (along the horizontal direction) after oxygen uptake, which is also confirmed by the refined average structure. O–O distances around 2.5–3.0 Å are shortened after oxidation, implying that the crowding among the oxygens is due to oxygen insertion. It is also noted that the relative O–O pair intensities of $LnFeMnO_{4.5}$ are enhanced compared with $LnFeMnO_4$, confirming more oxygen atoms are accommodated into the structure after oxygen uptake. The x-ray PDFs of $LnFeMnO_4$ and $LnFeMnO_{4.5}$ (Ln = Yb and Lu) are shown in Figs. S3 and S7. The M-O and O–O pairs are much less obvious compared with the neutron PDFs due to the insensitivity of oxygen compared with neutron scattering. However, we do confirm from x-ray PDFs that the observable atomic distances along the c-direction are shortened after the oxygen uptake, consistent with the Raman and Rietveld results.

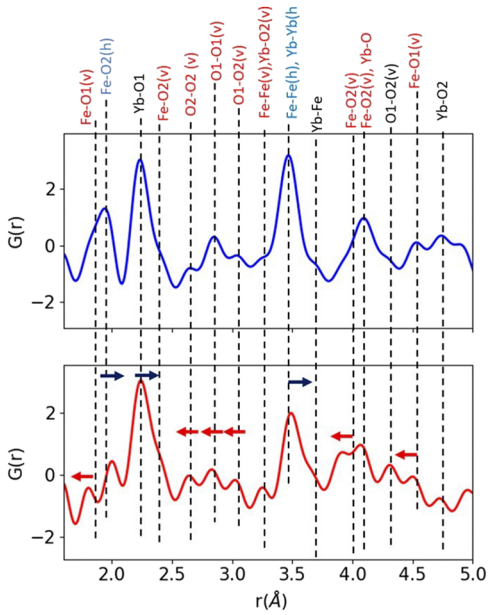

FIG. 4. Neutron pair distribution function (PDF) comparison between $YbMnFeO_4$ (top) and $YbMnFeO_{4.5}$ (bottom).

C. Satellite reflections from structural modulations

To better understand the structural differences between $LnFeMnO_4$ and $LnFeMnO_{4.5}$, high-resolution TEM (HRTEM) imaging and electron diffraction (ED) were performed on powder grains (Fig. 5 for Ln = Yb). The orientations of the ED patterns were determined based on the simulated electron diffraction (ED) patterns of the refined crystal structures (Figs. S11 and S12). For the reduced phase $YbFeMnO_4$, we observed that most grains prefer to orient either along the [001] direction [Figs. 5(a) and 5(b)] or the [010] direction [Figs. 5(c) and 5(d)], suggesting that (001) and (010) are the preferred exposed facets for $YbFeMnO_4$.

The fast Fourier-transform (FFT) pattern converted from the HRTEM images and ED patterns also shows a hexagonal arrangement of diffraction spots, confirming the rhombohedral cells. The HRTEM image [Fig. 5(c)] along the incident electron beam of [010] direction shows a layered stacking fringe, consistent with the refined crystal structure where LnO octahedra layers and Fe/MnO bipyramid double layers are alternatively stacked. It is reported that satellite peaks can be observed in the ED patterns for $LnFe_2O_4$ due to the charge ordering of Fe^{2+} and Fe^{3+}.[15,17,53,54] However, in our case of YbFeMnO4, there is no charge ordering because the Mn^{2+}/Fe^{3+} pair is much more energy-favored than the Fe^{2+}/Mn^{3+} pair.[18,55]

After oxygen uptake, the major Bragg diffraction spots along the [001] direction maintain the hexagonal arrangement, whereas those along the [110] direction remain vertically aligned, confirming the unchanged rhombohedral unit cell ($a = b$, $\alpha = \beta = 90°$, and $\gamma = 120°$) after oxidation. HRTEM image [Fig. 5(g)] along the incident electron beam of [110] direction also shows a layered stacking fringe, indicating that the stacked layered framework persists after oxygen uptake. We also realized that most grains are now either oriented along the [001] direction [Figs. 5(e) and 5(f)] or the [110] direction [Figs. 5(g) and 5(h)] after the oxidation, which implies that the (110) planes observed in the oxidized phase are transformed from the (010) planes in the reduced phase. This transformation strengthens the argument that the structural transition from $YbFeMnO_4$ to $YbFeMnO_{4.5}$ is through the mechanism of layer shift along the *ab* directions.

Apart from the major reflections in the ED patterns for $YbFeMnO_{4.5}$, satellite reflections are noted in both [001] and [110]

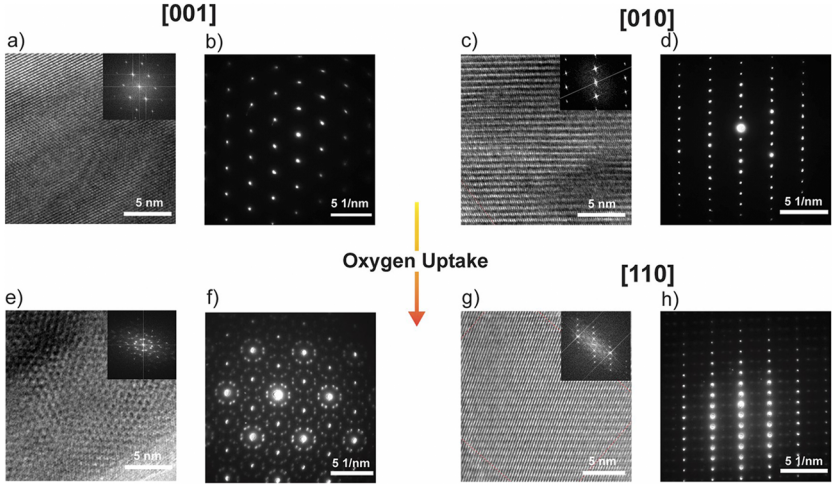

FIG. 5. (a) HRTEM image and (b) ED pattern of $YbFeMnO_4$ along the incident electron beam of [001]. (c) HRTEM image and (d) ED pattern of $YbFeMnO_4$ along the incident electron beam of [010]. (e) HRTEM image and (f) ED pattern of $YbFeMnO_{4.5}$ along the incident electron beam of [001]. (g) HRTEM image and (h) ED pattern of $YbFeMnO_{4.5}$ along the incident electron beam of [110].

directions [Figs. 5(f) and 5(h)]. The existence of satellite reflections is clearly an indication of structural modulations, which is consistent with the observed satellites in both synchrotron x-ray and neutron diffraction. In the [001] direction [Fig. 5(f)], each main Bragg diffraction spot was surrounded by 12 satellite spots. We interpret this number of satellites as a pair of reflections at each hexagonal edge with some angle of splitting. The symmetric arrangement of the satellites implies a modulation vector $\boldsymbol{q}$ of high symmetry. In the [110] direction [Fig. 5(h)], the additional superlattice spots were observed within the two main Bragg diffraction spots and were horizontal to the main $(\bar{1}01)$ Bragg diffraction spot with a modulation wave vectors $\boldsymbol{q}$ = (0, 1/3, and 0), suggesting that the modulation is 2D and propagates within the *ab*-plane [*q*= (a, b, and 0)]. Interestingly, the structural modulation seems so strong that it can be rendered in real-space HRTEM images. Both Figs. 5(e) and 5(g) show aperiodic structures with a nanometer scale apart from the atomic arrangement. The satellites are also visible in the FFT patterns [Figs. 5(e) and 5(g) inserts]. The observed HRTEM images and ED patterns are highly identical, regardless of the Ln site elements. Figures S14 and S15 show HRTEM images and ED patterns of $LuFeMnO_4$ and $YFeMnO_4$ before and after oxidation. The satellite Bragg diffraction spots appearing in the ED patterns of oxidized phases along [001] and [110] directions are highly identical to what is observed on $YbFeMnO_{4.5}$, showing a 12-direction and highly symmetric structural modulation that propagates within the *ab*-plane.

Structural modulation is reported on $LuFe_2O_{4.5}$ and $YbFe_2O_{4.5}$ as well. However, the observed propagation of structural modulation in $LnFe_2O_{4.5}$ shows a great deviation from what we observed on $LnFeMnO_{4.5}$. In the $LnFe_2O_{4.5}$ system (Ln = Yb and Lu), the structural modulation is reported to propagate along *ac* and *bc* planes [modulation wave vectors $\boldsymbol{q}$ = (a, 0, c)].[26,27,29] In addition, only 6 instead of 12 propagation directions of the modulation are observed in their ED patterns.[26,27,29]

D. Magnetic properties

The magnetic properties of reduced phase $LnFeMnO_4$ and oxidized phase $LnFeMnO_{4.5}$ are investigated through magnetic susceptibility and neutron diffraction measurements. Susceptibility measurement of $YbFeMnO_4$ has been previously reported, and our results on $YbFeMnO_4$ display similar behavior.[18] The DC susceptibility from 2 to 300 K (Fig. S16a) shows that the reduced phase $YbFeMnO_4$ displays an antiferromagnetic transition around 65 K. The Curie-Weiss fit (250–300 K, Fig. S16b) provides an effective moment size of 4.02 u_B, per formula unit, which deviates significantly from the theoretical value of 11.8 u_B based on the addition of all three magnetic atoms (one Mn^{2+}, one Fe^{3+}, and one Yb^{3+}). This deviation suggests that there are still strong magnetic correlations among the magnetic ions of $YbFeMnO_4$ even at room temperature.

The AC susceptibility measurements [Figs. 6(a) and 6(b)] show that the antiferromagnetic transition temperature varies when different frequencies are applied. We calculated the value of $\Delta T/T/\Delta \log f$ to be 0.007 (where ΔT = peak shift, T = peak temperature, and $\Delta \log f$ = difference of the logarithm of frequency). This calculated value is close to the minimum one for spin glassy systems (~0.004).[56] In the imaginary part (χ'') for $YbFeMnO_4$, a broad peak or shoulder was also observed below T_f (around 30 K) and was found to shift with changing the frequency, which may be related to the anisotropic spin freezing.[57,58]

Time of flight powder neutron diffractions at 300, 100, 40, and 5 K on $YbFeMnO_4$ are presented in Fig. 6(c). We did not observe any structural transition from 300 to 5 K as the diffraction peaks from the nuclear component remain nearly identical across the whole temperature range. PDFs from 5 to 300 K do not show any major deviations either (Figs. S20 and S21). However, broad magnetic peaks at Q = 1.25 $Å^{-1}$ and Q = 2.5 $Å^{-1}$ grow upon cooling. The magnetic peaks appear even at room temperature, implying a strong magnetic correlation, which is consistent with the DC susceptibility analysis. We noted the magnetic peaks are considerably broad and highly asymmetric, suggesting the magnetic ordering is short range and two-dimensional.[59–61] We indexed the magnetic peaks as the (1/3, 1/3, *l*) and (2/3, 2/3, *l*).

After oxidation to $YbFeMnO_{4.5}$, the magnetic properties significantly altered. DC susceptibility measurements from 2 to 300 K (Fig. S16) indicate $YbFeMnO_{4.5}$ also displays an antiferromagnetic transition, however, at a much lower temperature (around 30.5 K compared with 62 K for $YbFeMnO_4$). The moment gained from the Currie-Weiss fit is 15.61 u_B per formula, still deviating from the theoretical value (15.3 u_B: one Mn^{3+}, one Fe^{3+}, one Yb^{3+}). AC susceptibility measurements [Figs. 6(d) and 6(e)] show that this antiferromagnetic transition temperature varies when different frequencies are applied. We calculated $\Delta T/T/\Delta \log f$ to be 0.0066, still very close to the minimum value for spin glass systems. In the imaginary part (χ'') for $YbFeMnO_{4.5}$, a relatively broad peak except for the peak for T_f was also observed around 10 K and was found to shift with changing the frequency [Fig. 6(e)].

Time of flight powder neutron diffraction at 300, 10, 40, and 5 K on $LuFeMnO_{4.5}$ are presented in Fig. 6(f). Similar to $YbFeMnO_4$, no nuclear structural transition is observed from 300 to 5 K (also true for the PDFs at 5 and 300 K). A magnetic peak is still visible at Q = 1.25 $Å^{-1}$ even at room temperature, but more diffuse compared with $YbFeMnO_4$.

We found that the Ln site element has minimal influence on the magnetic properties of the reduced phase $LnFeMnO_4$ and the oxidized phase $LnFeMnO_{4.5}$. The same magnetic susceptibility and temperature-dependent neutron diffraction measurements were performed on the Ln = Lu and Y samples, and the results are provided in Figs. S16–S18. Important parameters gained from the magnetic measurements are listed in Table S7. All $LnFeMnO_4$ and $LnFeMnO_{4.5}$ show spin-glass behavior. The effective moments from Curie-Weiss fits never agree with the theoretical values based on isolated moments. In the neutron datasets, the reduced phases of $LnFeMnO_4$ all show broad and highly asymmetric magnetic peaks upon cooling. The positions of the magnetic peaks can be indexed into (1/3, 1/3, *l*) and (2/3, 2/3, *l*), regardless of the Ln cations. Upon oxidation, magnetic peaks become much less visible, and there is a decrease in temperature for the antiferromagnetic transition.

IV. DISCUSSION

A. Lattice contraction upon oxidation

Table I compares the normalized lattice parameters and some of the special distances within the crystal structure of $LnFeMnO_4$ before and after oxygen uptake. The refined lattice parameters indicate that for all $LnFeMnO_4$ (Ln = Y, Lu, and Yb) samples, oxygen

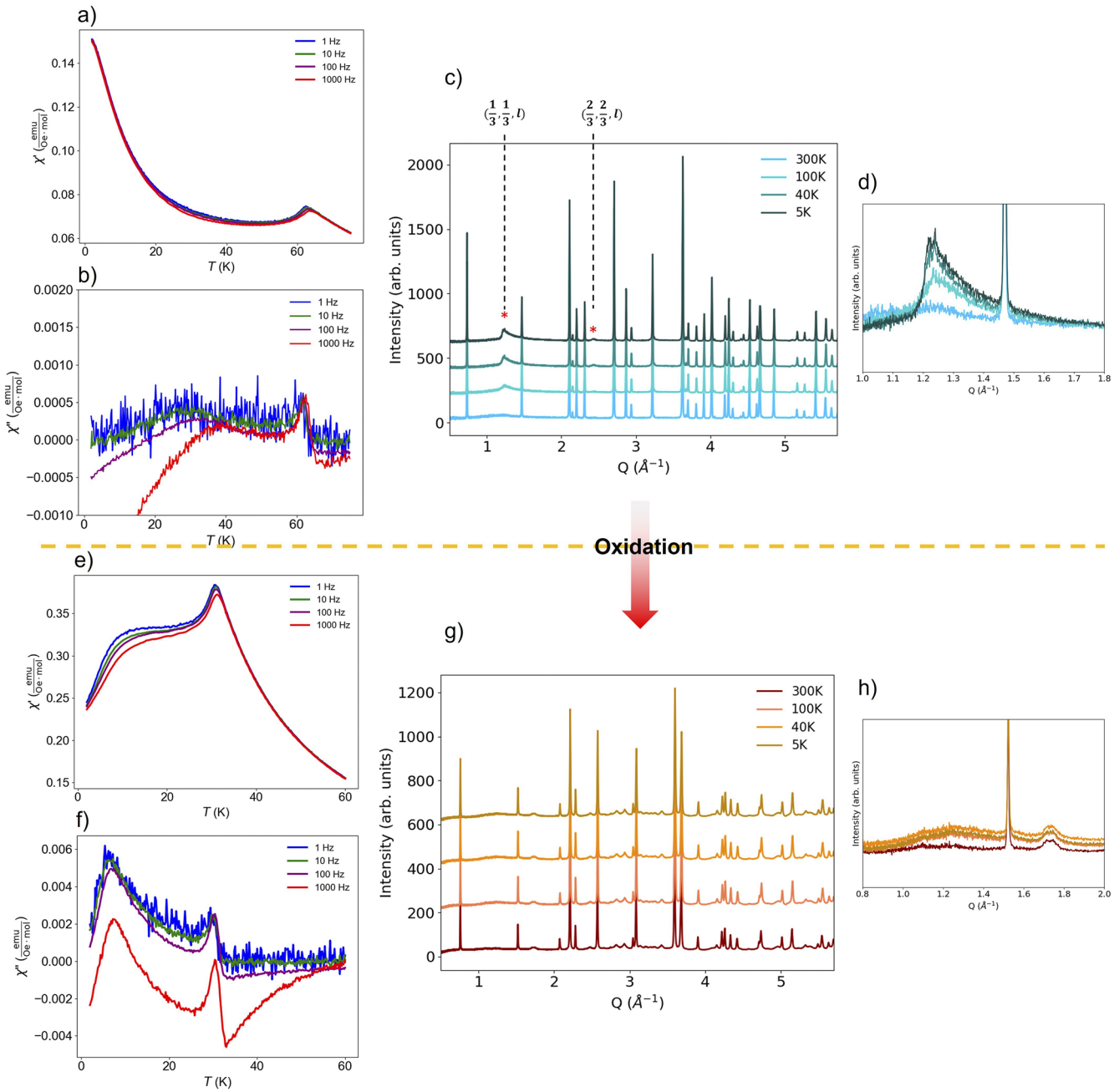

FIG. 6. AC susceptibility (a) real component and (b) imaginary component of $YbFeMnO_4$. (c) Temperature dependent neutron diffraction of direction of $YbFeMnO_4$ and (d) Zoom-in magnetic peaks. AC susceptibility (e) real component and (f) imaginary component of $YbFeMnO_{4.5}$. (g) Temperature dependent neutron diffraction of direction of $YbFeMnO_{4.5}$ and (h) zoom-in magnetic peaks.

uptake leads to contraction along the c-direction. Measuring the thickness of the LnO octahedra layer and the Fe/MnO bipyramid double layer, we found out the Fe/Mn bipyramid double layer undergoes contraction, whereas the LnO octahedra layer expands after the oxygen uptake, as shown in Table I. Thus, the contraction of the c-lattice parameter of the oxidized phase is mainly a result of the contraction of Fe/MnO bipyramid double layers. Previous studies show the oxidation of $LnFe_2O_4$ (Ln = Y, Lu, and Yb) leads to the expansion along c-directions,[26,29,30] which is opposite to what we have observed on $LnFeMnO_4$, as presented in Fig. 7.

TABLE I. Sublayer thickness and special bond distance of $LnFeMnO_4$ and $LnFeMnO_{4.5}$ (*O2–O3 and O3–O3 distance only exist in the oxidized phase $LnFeMnO_{4.5}$. ** parameters for $LnFeMnO_{4.5}$ are based on the average structure).

	Sublayer thickness (Å)		Bond distance (Å)			
Material	MO polyhedral double layer	LnO octahedra layer	M-M vertical	M-M horizontal	O2–O3 *	O3–O3 *
$LuMnFeO_4$	6.226	2.346	3.276	3.444		
**$LuMnFeO_{4.5}$	5.815	2.436	3.173	3.478	2.152	2.529
$YbMnFeO_4$	6.231	2.304	3.25	3.459		
**$YbMnFeO_{4.5}$	5.756	2.488	3.175	3.488	2.169	2.488
$YMnFeO_4$	6.167	2.32	3.194	3.496		
**$YMnFeO_{4.5}$	5.722	2.523	3.168	3.519	2.059	2.561

The oxygen uptake of $LnFeMnO_4$ correlates with the oxidation of Mn^{2+} (d^5) into Mn^{3+} (d^4) within the structure, whereas the oxygen uptake of $LnFe_2O_4$ correlates with the oxidation of Fe^{2+}(d^6) into Fe^{3+}(d^5). The different electron configuration changes upon oxidation (d^5 to d^4 for oxidation of $LnFeMnO_4$ and d^6 to d^5 for oxidation of $LnFe_2O_4$) can influence the crystal field effect in the Mn/FeO_5 bipyramid,[32,62] causing opposite lattice expansion behaviors for $LnFeMnO_4$ and $LnFe_2O_4$.

B. Oxygen insertion mechanism

The oxygen uptake of $LnFeMnO_4$ into $LnFeMnO_{4.5}$ leads to the insertion of extra oxygen into the crystal lattice. The average structure of $LnFeMnO_{4.5}$ [Fig. 1(d)] indicates that the extra oxygens (O3) are located in between the Fe/Mn–O double layer. Based on such an observation, intuitively, we can infer that the oxygen insertion process on $LnFeMnO_{4.5}$ should happen in between the Fe/Mn–O bipyramid layers [in the middle of the Fe/Mn–O bipyramid double layer, close to the lattice plane (002)].[29] If this proposed mechanism is correct, at the early stage of oxygen uptake of $LnFeMnO_4$, where the oxygen uptake is far smaller than 0.5, the inserted oxygen atoms should exist between the Fe/Mn–O bipyramid layers as interstitial oxygen before the phase transition occurs. To further verify this proposed insertion mechanism, the bond valence summation approach[63,64] was applied to the reduced phase $LnFeMnO_4$ to estimate the relative energy of the interstitial oxygen ions at different locations. The program softBV is commonly used to estimate the migration pathways for ions based on the energy of the sites estimated from the bond valence summation.[65,66] The calculated energy of sites can also be used to estimate the preferred occupying sites of certain ions. Figure 8 displays the sites for interstitial oxygen (position coordinates are included in Table S8), which are calculated to have the lowest energy. We clearly observe that the possible low-energy interstitial oxygen sites are all concentrated in between the Fe/Mn–O bipyramid layers, suggesting that the oxygen insertion in between the Fe/Mn–O bipyramid layers is the most energy favorable.

Bond valence summation analysis also indicates that the Mn/Fe sites are under-bonded in $LnFeMnO_4$. The bond valence sum of the Mn/Fe site is calculated to be around +2.25 compared with the

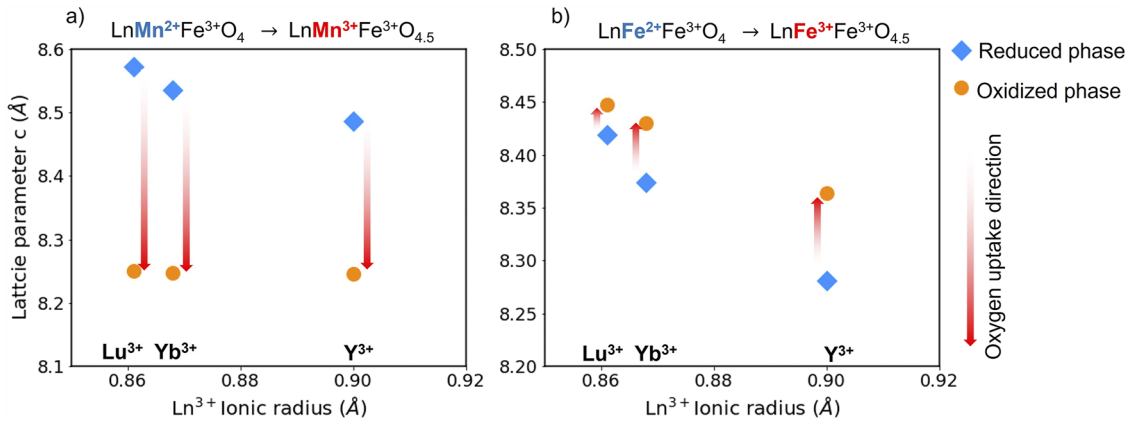

FIG. 7. (a) c lattice parameter comparison of $LnFeMnO_4$ before and after oxygen uptake. (b) c lattice parameter comparison of $LnFe_2O_4$ before and after oxygen uptake.

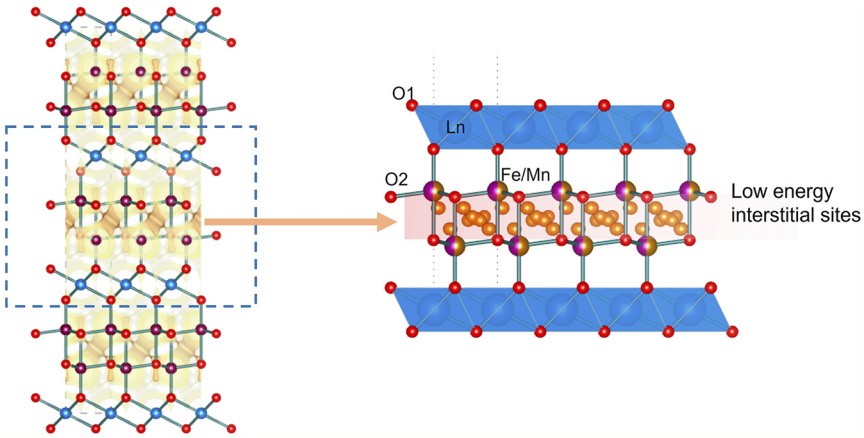

FIG. 8. Energy favored oxygen interstitial sites in reduced phase $LnFeMnO_4$ calculated by softBV.[65,66] In the structure on the left, the darker the yellow color, the lower energy for interstitial oxygen to occupy and the higher chances for the interstitial oxygen to appear at the early stage of oxygen uptake for $LnFeMnO_4$.

theoretic value of +2.5. This under-bonded environment in $LnFeMnO_4$ potentially allows the Mn/Fe site to bond extra oxygen atoms under oxidation conditions.

C. Structural modulation of the oxidized phase $LnFeMnO_{4.5}$

Structural modulation upon oxidation of $LnFe_2O_4$ into $LnFe_2O_{4.5}$ has been recently reported.[26,27,29] Also, it was shown that the propagation of modulation changes in $LuFe_2O_4$, depending on how much oxygen the material can uptake.[26,28] Our study only focuses on the fully oxidized phase $LnFeMnO_{4.5}$. As mentioned previously, $YFeMnO_{4.5}$, $LuFeMnO_{4.5}$, and $YbFeMnO_{4.5}$ possess similar modulation structures as they all show a similar arrangement of satellite peaks in the diffraction patterns. Figures 9(a) and 9(b) show the enlarged ED patterns of $YbFeMnO_{4.5}$ from Figs. 5(f) and 5(h), respectively. The 12 modulation vectors can be clearly seen in Fig. 9(a). Since direction does not change between the real space and reciprocal space, the direction of modulations can be visualized in the real crystal structure based on the direction of satellites in the electron diffraction. Figure 9(c) presents the top view (from the *c*-direction) of the $YbFeMnO_{4.5}$ average structure lattice, with the direction of modulation vectors indicated. We note that the directions of the 12 modulations are indeed identical in the average structure.

The angle between the wave vector $\boldsymbol{q}$ and *a*-axis is measured to be around 19°, aligned with the diagonal line of the two-unit cells [shown in Fig. 9(c)]. The modulation wave vector $\boldsymbol{q}$ is measured to be (−0.28, 0.14, and 0), close to the commensurate vector (−2/7, 1/7, 0). Assuming that it is indeed commensurate, the 12 modulation vectors are measured to be (−2/7, 1/7, 0), (1/7, −2/7, 0), (3/7, 1/7, 0), (3/7, 2/7, 0), (2/7, 3/7, 0), (1/7, 3/7, 0), (−3/7, −1/7, 0), (−3/7, −2/7, 0), (−2/7, −3/7, 0), (−1/7, −3/7, 0), (2/7, −1/7, 0), and (1/7, −2/7, 0).

Our observed ED patterns are homogeneous in the samples, as all tested crystalline grains show the same results. From these observations, we quickly realized that all 12 modulation wave vectors can be generated through symmetry operations from the $P\bar{3}m1$ space group (symmetry operations of $P\bar{3}m1$ are listed in Table S9)[67] on wave vector $\boldsymbol{q}$. However, applying symmetry operations from $P\bar{3}$ space group (symmetry operations of $P\bar{3}$ are listed in Table S9) on wave vector $\boldsymbol{q}$ can only generate six identical modulation wave vectors, in which case, two independent modulation wave vectors $\boldsymbol{q}$ = (−2/7, 17, 0) and $\boldsymbol{q}'$ = (−17, 2/7, 0) are necessary to describe the structural modulations. From the symmetry of the modulation vectors, $P\bar{3}m1$ seems to be a better choice for describing the average structure of $LnFeMnO_{4.5}$. However, it is rare but might be possible that the modulation wave vectors $\boldsymbol{q}$ = (−2/7, 1/7, and 0) and $\boldsymbol{q}'$ = (−1/7, 2/7, and 0) are twined, in which case, $P\bar{3}$ will be a better choice for describing the average structure of $LnFeMnO_{4.5}$.

Although $LnFe_2O_{4.5}$ also shows structural modulations,[26,27,29] the observed modulation wave vectors of $LnFe_2O_{4.5}$ (Ln = Lu and Fe) are in great difference with our $LnFeMnO_{4.5}$ system. $LuFe_2O_{4.5}$ show a modulation wave vector (0.31, 0, and 0.33)[26] and $YbFe_2O_{4.5}$ show a modulation wave vector (0.31, 0, and 0.33),[29] both of which propagate within *bc*- and *ac*-planes rather than the *ab*-plane. The multiplicity of the modulation wave vector observed in $LuFe_2O_{4.5}$ and $YbFe_2O_{4.5}$ is less than that of the $LnFeMnO_{4.5}$ system, indicating a lower symmetry for the structural modulations. Since $LnFe_2O_{4.5}$ and $LnFeMnO_{4.5}$ show nearly identical average structures, the ultimate reason for their very different modulation vectors is not clear. We previously noted that the oxidation in $LnFe_2O_4$ leads to *c*-direction expansion,[26,29] whereas oxidation in $LnFeMnO_4$ to $LnFeMnO_{4.5}$ leads to *c*-direction contraction. Likely that different anisotropic lattice expansion behavior upon oxidation is correlated with the different structural modulations.

We further refined the structural modulation of $LnFeMnO_{4.5}$ with the powder diffraction data. Although the measured modulation wave vector from ED results seems to be a commensurate value, treating the structure as a commensurate case would have required building a 7 × 7 supercell, which can be extremely complex. Thus, here, we approximate the structural modulation as an incommensurate case and apply the superspace approach.[45,46] The modulation wave vectors are indexed and refined on both synchrotron and neutron diffractions. Figures 9(d) and 9(e) show the refinement

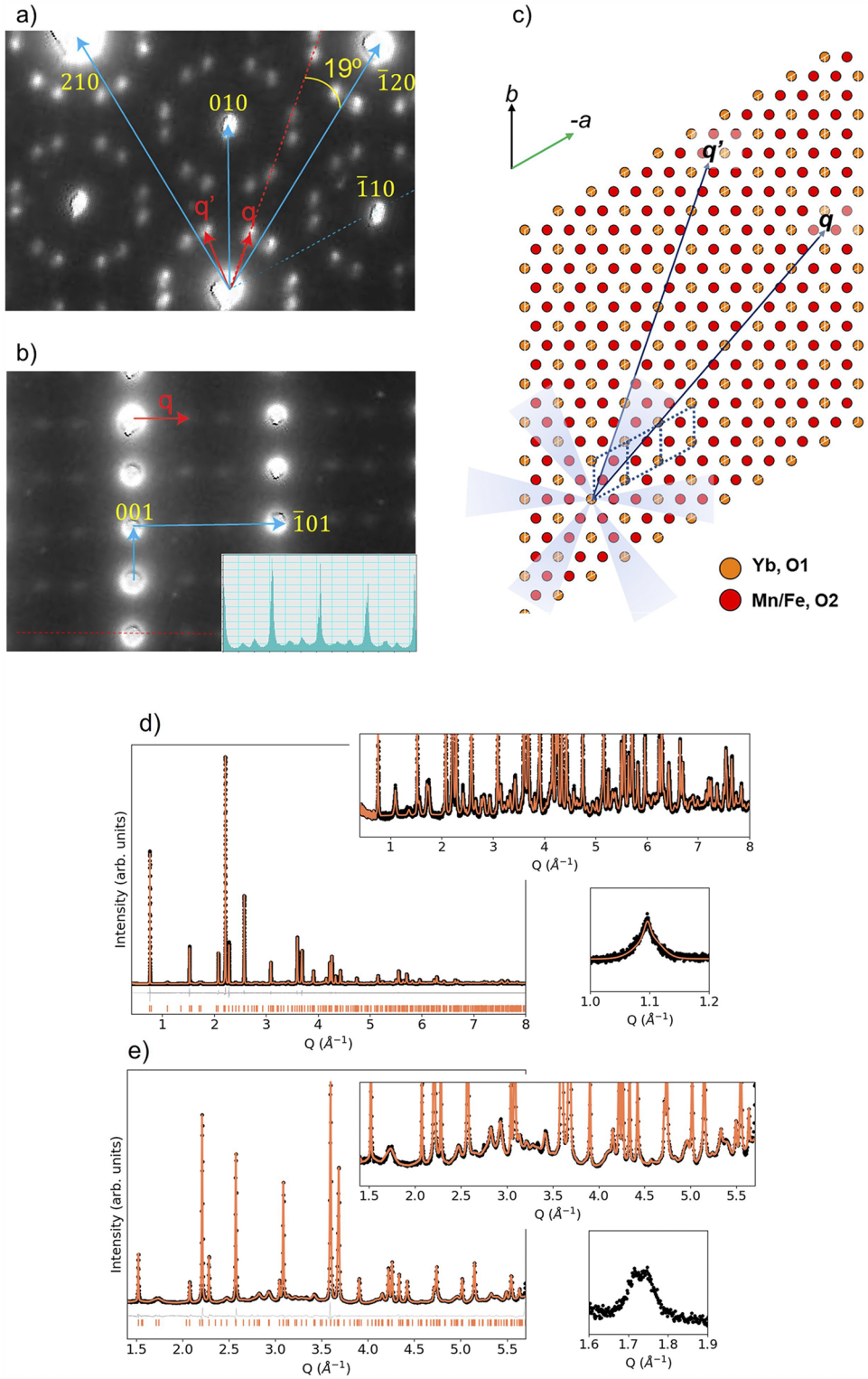

FIG. 9. Analysis of modulation vector from electron diffraction patterns in (a) [001] direction and (b) [110] direction (diffraction peak profile shown in inset). (c) Display of the modulation vector in the real space structure in [001] direction. Refinement of modulation wave vector with (d) synchrotron x-ray and (e) neutron diffractions of $YbFeMnO_{4.5}$. Subsets show the zoom in satellite peaks.

of $YbFeMnO_{4.5}$ with SXRD and NPD data. The refinements of $LuFeMnO_{4.5}$ and $YFeMnO_{4.5}$ are displayed in Figs. S21–S24. Here, we only applied one modulation wave vector $\boldsymbol{q}$= (1/7, 3/7, and 0) with $P\bar{1}(ab0)$ group, and we can see that is already enough to account for all the positions of satellite peaks, confirming the symmetric nature of 12 modulation vectors. The indexed and refined modulation vectors from powder diffractions are listed in Table II, which are in good agreement with ED. We also note that those satellite peaks in the powder diffraction patterns display extreme Lorentzian broadening features [Figs. 9(d) and 9(e)], suggesting that the modulation is not continuous across whole crystal grains but has nano-size domains.

Due to the existence of stacking faults and small domains of structural modulation, solving the modulation structure of $LnFeMnO_{4.5}$ from only powder diffraction is extremely challenging. Thus, we aimed to qualitatively understand the modulation rather than fully solve the modulations. To alleviate the complexity modulation refinement, $P\bar{1}(ab0)$ group was used, and only modulation along one $\boldsymbol{q}$ vector (1/7, 3/7, and 0) was refined. We also assumed the modulation along other modulation vectors should be symmetric or centrosymmetric to the modulation along one $\boldsymbol{q}$ vector (1/7, 3/7, and 0). We mainly used $YbFeMnO_{4.5}$ to perform analysis for understanding, as the quality of diffraction patterns of $LuFeMnO_{4.5}$ and $YFeMnO_{4.5}$ are lower due to much more severe stacking faults. For SXRD, we only refined the modulation of Ln and Fe/Mn sites as x-ray is not sensitive to oxygen. For NPD of $YbFeMnO_{4.5}$, the Yb, Fe/Mn, and all O sites were refined. The refinement on $LuFeMnO_{4.5}$ was also attempted. The displacive modulation along *a, b,* and *c* for Yb, Fe, and oxygen atoms are shown in Figs. S25–S39, which is refined from neutron diffraction of $YbFeMnO_{4.5}$. The refined modulation parameters are listed in Tables S10–S13.

Figure 10 shows a displacive modulation of O1, Fe/Mn, O3, and O2 sites along the c-direction. The Yb, Fe/Mn, and O1 sites all show strong periodic displacement along the modulation vector. Displacement of Fe and O1 along the c direction is relatively strong. We noted that the modulation curves for Fe/Mn and O1 along the c-direction have a phase difference of t/2, causing periodic breathing of Fe–O1 bonds, whereas O2 and O3 are partially occupied. Their occupancy periodicities also show a phase difference of roughly t/2, suggesting that O2 and O3 do not appear in the same unit cell. In the average structure of $LnFeMnO_{4.5}$, the distance between O2 and O3 is around 2–2.2 A (Table I), which is far smaller than two times the radius of the O^{2-} anion (2.4–2.8 A).[68] The alternate occupancy of O2 and O3 makes physical sense as the occupancy at the same unit cell of O2 and O3 would cause a covalent overlap. Since structure has an inversion center, inversion of the modulation of O3 shows that the periodicity of the occupancy of O2 and O3 inversion sites will have a t/2 phase shift. The phase shift of the inversion sites O3′ (or O2′) indicates that O3′ and O3 should probably not appear in the same unit cell either. Since modulation appears after oxygen insertion, it is likely that the ordering of oxygen vacancy ordering is one of the major drivers for the structural modulations.

TABLE II. Measured/indexed modulation vector of $LnFeMnO_{4.5}$ from electron, x-ray, and Neutron diffractions.

	Electron diffraction	X-ray	Neutron
$LuFeMnO_{4.5}$	(0.14, 0.42, 0)	(0.1429, 0.4287, 0)	(0.1437, 0.4311, 0)
$YbFeMnO_{4.5}$	(0.14, 0.42, 0)	(0.1433, 0.4299, 0)	(0.1431, 0.4293, 0)
$YFeMnO_{4.5}$	(0.14, 0.42, 0)	(0.1445, 0.4335, 0)	(0.1435, 0.4305, 0)

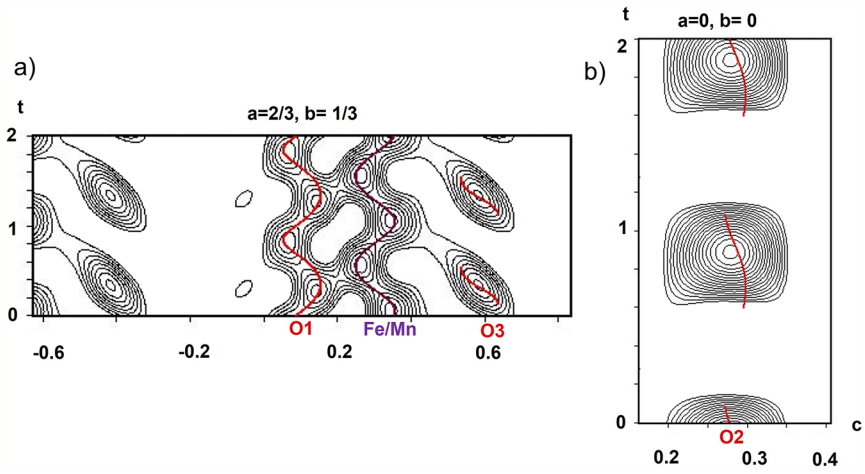

FIG. 10. (a) Displacive modulation of O1, Fe/Mn, and O3 site along c direction. O1, Fe/Mn, and O3 are shown together since they have the same x and y coordinates (1/3, 2/3, and z). (b) Displacive modulation of O2 site along c direction. t represents modulation period.

D. Short-range magnetic correlations

The magnetic properties of $YFeMnO_4$ have been previously studied.[60,61,69,70] The AC susceptibility suggests that $LnFeMnO_4$ shows a weak spin glass-like state with the spin freezing transition. Our temperature-dependent neutron diffraction indicates that 2D short-range magnetic ordering exists in $LnFeMnO_4$, regardless of Ln. Following the order of Ln = Y, Yb, and Lu, as the c-lattice parameter increases, the spin-frozen transition temperature decreases slightly increases (Table S7), suggesting the dominant magnetic interaction might be along the ab-plane rather than the c-direction.

Magnetization measurement on single crystal $YFeMnO_4$ at 4.2 K shows an anisotropic ferrimagnetic behavior of $YFeMnO_4$. A larger magnetic hysteresis loop was observed on $YFeMnO_4$ parallel to c-direction than vertical to it. Two-dimensional ferrimagnetic ordering is also observed in the $LnFe_2O_4$ systems.[14,71,72] In the $LnFe_2O_4$ or $LnFeMnO_4$ systems, the Fe/Mn–O bipyramid double layers are separated by the Ln-O octahedral layers [shown in Fig. 1(c)], leading to extremely weak magnetic interactions between Fe/Mn–O bipyramid double layers in the c-direction.

The broad asymmetric magnetic diffraction peak observed in the $LnFeMnO_4$ system can be described with a warren line shape function:[73,74]

$$I(Q) = Kf_m^2F(a)\left[2Q\left(\frac{\lambda}{4\pi}\right) + Q^{\frac{1}{2}}\left(\frac{\lambda}{4\pi}\right)^{-2} - 2\right]\left(\frac{QL}{4\pi^{3/2}}\right)^{(1/2)},$$

where,

$$F(a) = \int_0^\infty \exp\left[-(x^2 - a)^2\right]dx,$$

and

$$a = L(Q - Q_0)/2\sqrt{2\pi},$$

Q_0 is the Q value of the center of the magnetic scattering, f_m the magnetic form factor, K scale factor, λ the incident wavelength of neutrons, and L the 2D spin-spin correlation length. The magnetic correlation lengths are extracted by fitting the (1/3, 1/3, l) magnetic peak at 5 K with a Warren line shape function. Figures 11(a)–11(c) present the fitting of this peak for $YFeMnO_4$, $LuFeMnO_4$, and $YbFeMnO_4$, respectively. The fitted magnetic correlation lengths are displayed in Table III. The magnetic correlation lengths of $LnFeMnO_4$ (Ln = Y, Lu, and Yb) are all around 10 nm, which is about 30 unit cells in length along the ab plane. However, the traditional Lorenz shape is not able to describe the magnetic peak shape here due to its asymmetric nature. Peak fitting with the Lorentz shape together with the instrument peak shape function was still attempted, and similar values for magnetic correlation length were gained. The magnetic correlation length fitted on $LnFeMnO_4$ is far smaller than what is reported on $LnFe_2O_4$ at around similar temperatures (e.g., 1 μm for $LuFe_2O_4$).[75]

Different from $LnFeMnO_4$, long-range 2D ferrimagnetic magnetic ordering develops upon cooling in $LnFe_2O_4$,[14,24,71,72,76] although the crystal structure and the location of the magnetic

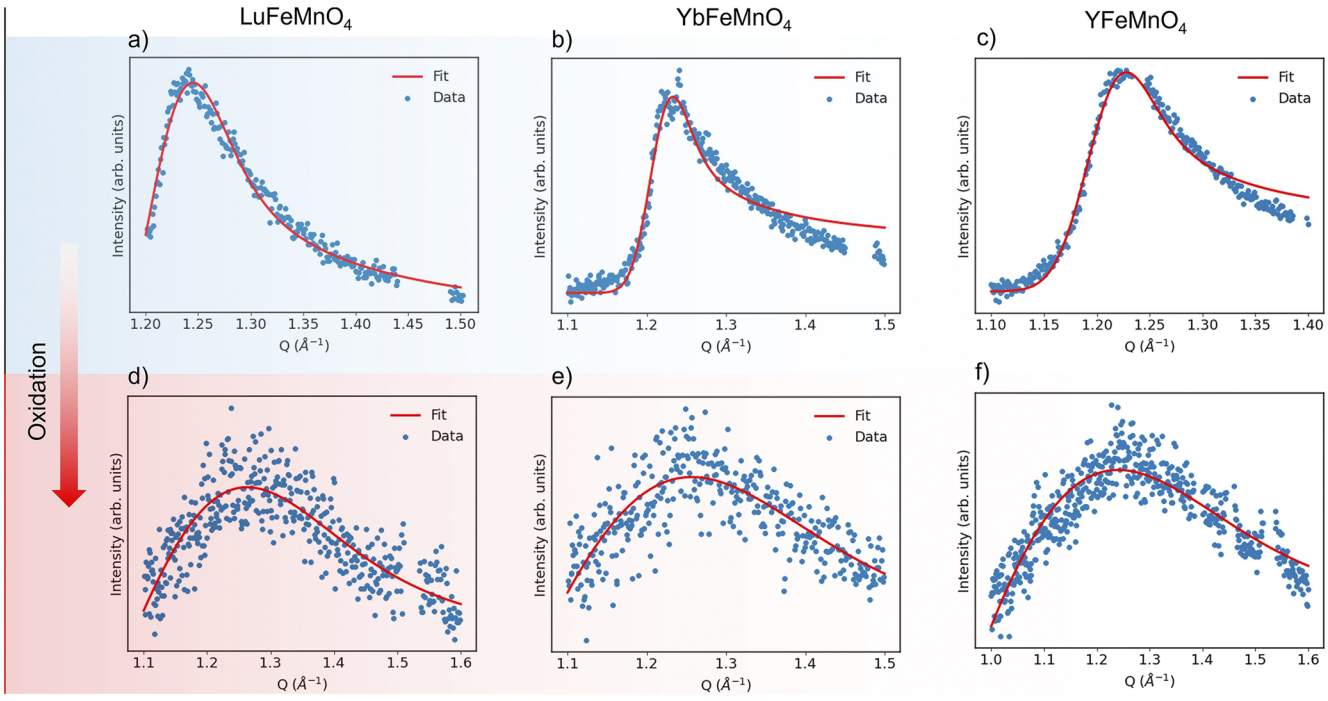

FIG. 11. Warren Line shape fitting of magnetic diffraction peak of (a)–(c) $LnFeMnO_4$ and (d)–(f) $LnFeMnO_{4.5}$.

TABLE III. Fitted magnetic correlation length of LnFeMnO4 before and after oxygen uptake.

Correlation length (Å)	Lu	Yb	Y
$LnFeMnO_4$	75.6	115.6	89.9
$LnFeMnO_{4.5}$	12.1	16.1	10.5

moments in the structure are identical for $LnFeMnO_4$ and $LnFe_2O_4$. The disordering of Fe^{3+} and Mn^{2+} is believed to contribute to the lack of long-range magnetic ordering in the $LnFeMnO_4$ system.[60,61] Charge ordering exists in the $LnFe_2O_4$ system, where $Fe^{2+}(d^6)$ and $Fe^{3+}(d^5)$ are located at different layers within the Fe–O bipyramid double layer.[15,49,71] For $LnFeMnO_4$, $Mn^{2+}(d^5)$ and $Fe^{3+}(d^5)$ are randomly distributed Fe/Mn–O bipyramid double layers due to the lack of charge order. However, we must note that both Fe^{3+} and Mn^{2+} in $LnFeMnO_4$ have the same electron configuration d^5 despite carrying different charges. Fe^{3+} and Mn^{2+} should possess the same magnetic dipole moment as they are in the same trigonal bipyramidal crystal field environment in the structure. The magnetic superexchange interaction thus should be the same on each Mn^{2+} or Fe^{3+} site despite charge disordering.

Figure 12 displays a qualitative analysis of the superexchange interaction in the $LnFeMnO_4$ system. Only the top and side views of the Fe/Mn–O bipyramid double layers are shown for simplicity. Two major superexchange pathways are indicated, J1 and J2. We write J1 between two Fe^{3+}/Mn^{2+} ions that are connected through two O^{2-} anions (M-O-M angle = 97.803°). Fe^{3+}/Mn^{2+} ions form the top and bottom bipyramid layers, respectively. We designate J2 between two Fe^{3+}/Mn^{2+} ions within the same bipyramid layer; hence, the cations are connected by only one O^{2-} ion (M-O-M angle = 118.2°). It is worth noting that J1 exactly aligns with the (1/3, 1/3, *l*) lattice plane, which is where the magnetic peak appears in the neutron diffraction patterns. However, we are unclear how the charge disorder influences other magnetic interactions other than through M-O-M superexchange.

Oxidation of $LnFeMnO_4$ into $LnFeMnO_{4.5}$ causes the decrease of the T_f from around 60–30 K, implying a weakening of the magnetic interactions between moments. We note that there is a *a*-lattice parameter expansion upon oxygen uptake of $LnFeMnO_4$ into $LnFeMnO_{4.5}$. The weakening of the superexchange interaction along the ab-plane may contribute to the decrease of T_f upon oxidation. It is also evident that oxygen uptake greatly suppresses the short-range magnetic ordering. Figures 11(d)–11(f) present the Warren line shape fitting on the magnetic peak (located at Q ~ 1.2 $Å^{-1}$) of $YFeMnO_{4.5}$, $LuFeMnO_{4.5}$, and $YbFeMnO_{4.5}$. The fitted magnetic correlation lengths are displayed in Table III. The magnetic correlation lengths of $LnFeMnO_{4.5}$ (Ln = Y, Lu, and Yb) are 1–2 nm, much shorter than that of $LnFeMnO_4$ (~10 nm). We consider several factors that cause the suppression of short-range magnetic ordering upon oxygen uptake of $LnFeMnO_4$. First, oxygen uptake leads to $Mn^{2+}(d^5)$ oxidation into $Mn^{3+}(d^4)$. The disordering of $Mn^{3+}(d^4)$ and $Fe^{3+}(d^5)$ cause the disordering of the different magnetic dipole moments. Second, the insertion of the extra O^{2-} changes the existing magnetic superexchange interactions. The new O^{2-} sites will undoubtedly connect some magnetic ions, which disturb the original ordered superexchange interactions. Finally, the displacement of Mn/Fe sites due to strong structural modulation in the oxidized phase can also disturb the originally ordered superexchange geometry.

Interestingly, in both reduced phase $YbMnFeO_4$ and oxidized phase $YbFeMnO_{4.5}$, their magnetic behavior does not differ from $LnMnFeO_4$ and $LnFeMnO_{4.5}$ (Ln = Y and Lu), although Yb^{3+} carries magnetic moment (4.5 μ_B in octahedra field),[77] but Y^{3+} and Lu^{3+} do not. It seems the YbO octahedra layer does not influence the spin-frozen states or the nature of the short-range magnetic order. This "non-involvement" of Yb^{3+} might be the result of magnetic frustration of the YbO octahedra layer. The severe displacement of Yb^{3+} in the structure and triangular arrangement of Yb^{3+} leads to strong magnetic frustration. Indeed, the isostructural $YbZnGaO_4$ and $YbMgGaO_4$ (where only Yb^{3+} carries moment) do not display

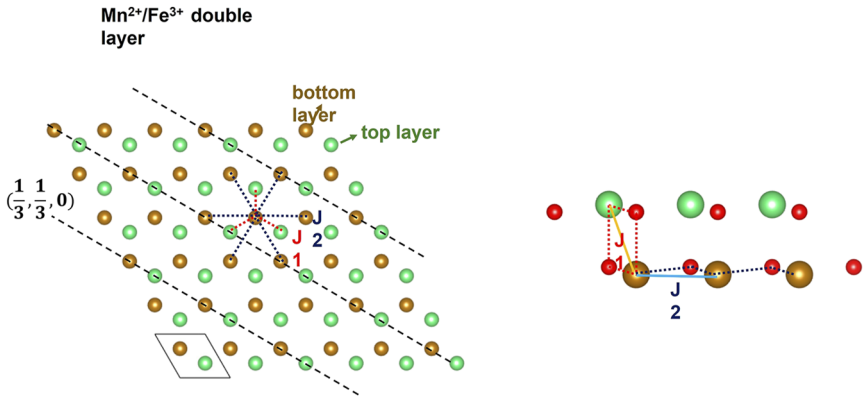

FIG. 12. Display of two major superexchange interaction between Fe/Mn–Fe/Mn ions in the $LnFeMnO_4$ structure in (a) [001] and (b) [100] directions. Green and yellow colors represent the same atom but in different layers.

any magnetic transition even at 2 K due to the magnetic frustration in the YbO octahedra layer.[12,78]

V. CONCLUSION

In summary, like $LnFe_2O_4$, $LnFeMnO_4$ displays an astonishing oxygen uptake behavior at low temperatures (~200 °C). Despite the similarity of the average crystal structure of fully oxidized phases, $LnFe_2O_4$ and $LnFeMnO_4$, the anisotropic lattice expansion behavior and structural modulations show significant variations. The change of the electron configuration of the transition metal upon oxidation (d^6 to d^5 for $LnFe_2O_4$, d^5 to d^6 for $LnFeMnO_4$) seems to play an important role in those differences. We also found that the oxidation of $LnFeMnO_4$ greatly suppresses its magnetic ordering. Our studies expand the $LnM^{2+}M^{3+}O_4$ family to oxygen storage materials. The modifiable nature of $LnM^{2+}M^{3+}O_4$ shows its potential to be tuned for many applications involving oxygen carriers such as chemical looping, catalytic oxidation/reduction, and oxygen ion conductors. The dramatic change of the physical property after the oxidation of $LnFeMnO_4$ suggests it can be used for oxygen gas sensing as well.

SUPPLEMENTARY MATERIAL

See the supplementary material for additional characterizations of $LnFe^{2+}Fe^{3+}O_4$ and $LnFe^{2+}Fe^{3+}O_{4.5}$ (where Ln = Y, Lu, and Yb) including refinement of average structure with Synchrotron x-ray and Neutron diffraction, TGA, Pair distribution function, Raman, TEM and magnetic susceptibility measurement. Crystal structure Refinement parameters are included. Crystal structure files (cif files) are provided.

ACKNOWLEDGMENTS

We acknowledge the NIST Cooperative Agreement Nos. 70NANB20H139 and 70NANB17H301 for support. Use of the Advanced Photon Source at Argonne National Laboratory was supported by the U.S. Department of Energy, Office of Science, Office of Basic Energy Sciences, under Contract No. DE-AC02-06CH11357. This research used resources at Spallation Neutron Source, a DOE Office of Science User Facility operated by the Oak Ridge National Laboratory. We thank M. Kirkham at POWGEN, SNS, and ORNL for her help with the powder neutron diffraction experiment.

AUTHOR DECLARATIONS

Conflict of Interest

The authors have no conflicts to disclose.

Author Contributions

Tianyu Li: Conceptualization (lead); Data curation (lead); Formal analysis (lead); Investigation (lead); Methodology (lead); Validation (lead); Visualization (lead); Writing – original draft (lead); Writing – review & editing (equal). **Sz-Chian Liou**: Formal analysis (supporting); Investigation (supporting); Writing – review & editing (supporting). **Stephanie J. Hong**: Writing – review & editing (supporting). **Qiang Zhang**: Investigation (supporting); Writing – review & editing (supporting). **H. Cein Mandujano**: Investigation (supporting); Writing – review & editing (supporting). **Efrain E. Rodriguez**: Conceptualization (supporting); Funding acquisition (lead); Methodology (supporting); Resources (lead); Supervision (lead); Validation (lead); Writing – review & editing (lead).

DATA AVAILABILITY

The data that support the findings of this study are available from the corresponding author upon reasonable request.

REFERENCES

[1] N. Kimizuka and T. Mohri, J. Solid State Chem. **60**, 382 (1985).
[2] N. Kimizuka and E. Takayama, J. Solid State Chem. **40**, 109 (1981).
[3] N. Kimizuka and T. Mohri, J. Solid State Chem. **78**, 98 (1989).
[4] R. Grajczyk and M. A. Subramanian, Prog. Solid State Chem. **43**, 37 (2015).
[5] N. P. Ong and R. J. Cava, Science **305**, 52 (2004).
[6] D. C. Cabra, C. A. Lamas, and H. D. Rosales, Phys. Rev. B **83**, 094506 (2011).
[7] Y. Li, H. Liao, Z. Zhang, S. Li, F. Jin, L. Ling, L. Zhang, Y. Zou, L. Pi, Z. Yang, J. Wang, Z. Wu, and Q. Zhang, Sci. Rep. **5**, 16419 (2015).
[8] J. A. M. Paddison, M. Daum, Z. Dun, G. Ehlers, Y. Liu, M. B. Stone, H. Zhou, and M. Mourigal, Nat. Phys. **13**, 117 (2017).
[9] Y. Li, Adv. Quantum Technol. **2**, 1900089 (2019).
[10] Y. Li, D. Adroja, R. I. Bewley, D. Voneshen, A. A. Tsirlin, P. Gegenwart, and Q. Zhang, Phys. Rev. Lett. **118**, 107202 (2017).
[11] W. Steinhardt, P. A. Maksimov, S. Dissanayake, Z. Shi, N. P. Butch, D. Graf, A. Podlesnyak, Y. Liu, Y. Zhao, G. Xu, J. W. Lynn, C. Marjerrison, A. L. Chernyshev, and S. Haravifard, npj Quantum Mater. **6**, 78 (2021).
[12] Z. Ma, J. Wang, Z. Y. Dong, J. Zhang, S. Li, S. H. Zheng, Y. Yu, W. Wang, L. Che, K. Ran, S. Bao, Z. Cai, P. Čermák, A. Schneidewind, S. Yano, J. S. Gardner, X. Lu, S. L. Yu, J. M. Liu, S. Li, J. X. Li, and J. Wen, Phys. Rev. Lett. **120**, 087201 (2018).
[13] S. Calder, S. R. Giblin, D. R. Parker, P. P. Deen, C. Ritter, J. R. Stewart, S. Rols, and T. Fennell, J. Phys.: Condens. Matter **25**, 356002 (2013).
[14] S. Katano, T. Matsumoto, S. Funahashi, J. Iida, M. Tanaka, and J. W. Cable, Physica B **213–214**, 218 (1995).
[15] N. Ikeda, H. Ohsumi, K. Ohwada, K. Ishii, T. Inami, K. Kakurai, Y. Murakami, K. Yoshii, S. Mori, Y. Horibe, and H. Kitô, Nature **436**, 1136 (2005).
[16] M. Angst, Phys. Status Solidi RRL **7**, 383 (2013).
[17] Y. Zhang, H. X. Yang, C. Ma, H. F. Tian, and J. Q. Li, Phys. Rev. Lett. **98**, 247602 (2007).
[18] K. Yoshii, N. Ikeda, T. Michiuchi, Y. Yokota, Y. Okajima, Y. Yoneda, Y. Matsuo, Y. Horibe, and S. Mori, J. Solid State Chem. **182**, 1611 (2009).
[19] K. Yoshii, M. Mizumaki, K. Matsumoto, S. Mori, N. Endo, H. Saitoh, D. Matsumura, T. Kambe, and N. Ikeda, J. Phys.: Conf. Ser. **428**, 012032 (2013).
[20] I. Nodari, A. Alebouyeh, J. F. Brice, R. Gérardin, and O. Evrard, Mater. Res. Bull. **23**, 1039 (1988).
[21] S. Cao, J. Lee, Z. Wang, H. Tian, Y. Qin, L. Zeng, C. Ma, H. Yang, and J. Li, Sci. Rep. **2**, 330 (2012).
[22] J. Akimitsu, Y. Inada, K. Siratori, I. Shindo, and N. Kimizuka, Solid State Commun. **32**, 1065 (1979).
[23] F. Wang, J. Kim, G. D. Gu, Y. Lee, S. Bae, and Y.-J. Kim, J. Appl. Phys. **113**, 063909 (2013).
[24] K. Fujiwara, T. Karasudani, K. Kakurai, W. T. Lee, K. C. Rule, A. J. Studer, and N. Ikeda, J. Phys. Soc. Jpn. **88**, 044701 (2019).
[25] F. Satoru, A. Jun, S. Kiiti, K. Noboru, T. Midori, and F. Hideshi, J. Phys. Soc. Jpn. **53**, 2688 (2013).

[26]M. Hervieu, A. Guesdon, J. Bourgeois, E. Elkaïm, M. Poienar, F. Damay, J. Rouquette, A. Maignan, and C. Martin, Nat. Mater. **13**, 74 (2014).
[27]M. Hervieu, F. Damay, A. Maignan, and C. Martin, Solid State Sci. **48**, A1 (2015).
[28]S. Deng, L. Wu, H. Cheng, J.-C. Zheng, S. Cheng, J. Li, W. Wang, J. Shen, J. Tao, J. Zhu, and Y. Zhu, Phys. Rev. Lett. **122**, 126401 (2019).
[29]S. Nicoud, M. Huvé, O. Hernandez, A. Pautrat, M. Duttine, A. Wattiaux, C. Colin, H. Kabbour, and O. Mentré, J. Am. Chem. Soc. **139**, 17031 (2017).
[30]R. S. Jayathilake, B. D. Levitas, and E. E. Rodriguez, J. Mater. Chem. A **6**, 4801 (2018).
[31]C. Blom, *Development of Rare Earth Metal Iron Oxides as Mixed Ionic and Electronic Conductors* (Norwegian University of Science and Technology, 2014).
[32]T. Li, R. Jayathilake, L. Balisetty, Y. Zhang, B. Wilfong, T. J. Diethrich, and E. E. Rodriguez, Mater. Adv. **3**, 1087 (2022).
[33]V. Petříček, V. Eigner, M. Dušek, and A. Čejchan, Z. Krist. **231**, 301 (2016).
[34]V. Petrícek, M. Dušek, and L. Palatinus, Z. Krist. **229**, 345 (2014).
[35]B. H. Toby and R. B. Von Dreele, J. Appl. Crystallogr. **46**, 544 (2013).
[36]G. Oszlányi and A. Süto, Acta Crystallogr., Sect. A **60**, 134 (2004).
[37]L. Palatinus and G. Chapuis, J. Appl. Crystallogr. **40**, 786 (2007).
[38]N. Kimizuka, A. Takenaka, Y. Sasada, and T. Katsura, Solid State Commun. **15**, 1321 (1974).
[39]M. Nespolo, M. Isobe, J. Iida, and N. Kimizuka, Acta Crystallogr., Sect. B **56** (Pt 5), 805 (2000).
[40]R. J. Cava, A. P. Ramirez, Q. Huang, and J. J. Krajewski, J. Solid State Chem. **140**, 337 (1998).
[41]R. F. Egerton, *Electron Energy-Loss Spectroscopy in the Electron Microscope* (Springer US, 2011).
[42]H. Kurata and C. Colliex, Phys. Rev. B **48**, 2102 (1993).
[43]M. J. Whelan and P. B. Hirsch, Philos. Mag. **2**, 1121 (1957).
[44]E. Estevez-Rams, M. Leoni, P. Scardi, B. Aragon-Fernandez, and H. Fuess, Philos. Mag. **83**, 4045 (2003).
[45]T. Janssen, A. Janner, A. Looijenga-Vos, and P. M. de Wolff, International Tables for CrystallographyVolume A: Space-group symmetry, edited by M. I. Aroyo (International Union of Crystallography, 2006).
[46]S. Van Smaalen, Crystallogr. Rev. **4**, 79 (1995).
[47]F. M. Vitucci, A. Nucara, D. Nicoletti, Y. Sun, C. H. Li, J. C. Soret, U. Schade, and P. Calvani, Phys. Rev. B **81**, 195121 (2010).
[48]X. S. Xu, J. De Groot, Q. C. Sun, B. C. Sales, D. Mandrus, M. Angst, A. P. Litvinchuk, and J. L. Musfeldt, Phys. Rev. B **82**, 014304 (2010).
[49]A. B. Harris and T. Yildirim, Phys. Rev. B **81**, 134417 (2010).
[50]A. Glamazda, K.-Y. Choi, P. Lemmens, D. Wulferding, S. Park, and S.-W. Cheong, Phys. Rev. B **87**, 144416 (2013).
[51]Y. Hou, Y. P. Yao, S. N. Dong, M. L. Teng, X. F. Sun, and X. G. Li, J. Raman Spectrosc. **42**, 1695 (2011).
[52]F. Sun, R. Wang, C. Aku-Leh, H. X. Yang, R. He, and J. Zhao, Sci. Rep. **4**, 6429 (2014).
[53]Y. Murakami, N. Abe, T. Arima, and D. Shindo, Phys. Rev. B **76**, 024109 (2007).
[54]S. Cheng, S. Deng, C. Xu, J. Tao, and Y. Zhu, Microsc. Microanal. **26**, 2546 (2020).
[55]J. Cazaux, J. Electron Spectrosc. Relat. Phenom. **113**, 15 (2000).
[56]J. A. Mydosh, *Spin Glasses: An Experimental Introduction* (CRC Press; Taylor & Francis, London, 1993).
[57]U. Atzmony, E. Gurewitz, M. Melamud, H. Pinto, H. Shaked, G. Gorodetsky, E. Hermon, R. M. Hornreich, S. Shtrikman, and B. Wanklyn, Phys. Rev. Lett. **43**, 782 (1979).
[58]M. Dragomir, P. A. Dube, I. Arčon, C. Boyer, M. Rutherford, C. R. Wiebe, G. King, H. A. Dabkowska, and J. E. Greedan, Chem. Mater. **31**, 7833 (2019).
[59]K. C. Rule, G. J. McIntyre, S. J. Kennedy, and T. J. Hicks, Phys. Rev. B **76**, 134402 (2007).
[60]J. Iida and Y. Nakagawa, J. Phys. Soc. Jpn. **59**, 4443 (1990).
[61]J. Iida, M. Tanaka, S. Funahashi, and Y. Nakagawa, J. Appl. Phys. **69**, 5801 (1991).
[62]H. A. Jahn and E. Teller, Proc. R. Soc. London., Ser. A **161**, 220 (1937).
[63]S. Adams and R. P. Rao, Struct. Bond. **158**, 129 (2014).
[64]S. Adams and R. P. Rao, Phys. Chem. Chem. Phys. **11**, 3210 (2009).
[65]H. Chen and S. Adams, IUCrJ **4**, 614 (2017).
[66]L. L. Wong, K. C. Phuah, R. Dai, H. Chen, W. S. Chew, and S. Adams, Chem. Mater. **33**, 625 (2021).
[67]T. R. Welberry, J. Appl. Crystallogr. **16**, 284 (1983).
[68]R. D. Shannon, Acta Crystallogr. Sect. A **32**, 751 (1976).
[69]M. Tanaka, J. Iida, E. Hiyama, and F. Shibata, Hyperfine Interact. **78**, 409 (1993).
[70]M. Tanaka, J. Iida, and K. Siratori, J. Alloys Compd. **192**, 75 (1993).
[71]H. Fujishita, J. Phys. Soc. Jpn. **53**, 2688 (1984).
[72]J. Iida, S. Kakugawa, G. Kido, Y. Nakagawa, S. Takekawa, and N. Kimizuka, Physica B Condens. Matter **155**, 307 (1989).
[73]S. F. Jin, Q. Huang, Z. P. Lin, Z. L. Li, X. Z. Wu, T. P. Ying, G. Wang, and X. L. Chen, Phys. Rev. B **91**, 094420 (2015).
[74]H. S. Nair, J. M. Brown, E. Coldren, G. Hester, M. P. Gelfand, A. Podlesnyak, Q. Huang, and K. A. Ross, Phys. Rev. B **97**, 134409 (2018).
[75]I. K. Yang, J. Kim, S. H. Lee, S. B. Kim, S. W. Cheong, and Y. H. Jeong, Appl. Phys. Lett. **106**, 152902 (2015).
[76]T. Müller, *Order and Disorder in the Charge and Spin Structures of* $YFe_2O_{4-\delta}$ *and* $Ni_{0.42}Mn_{0.58}TiO_3$ (RWTH Aachen University, 2018).
[77]R. M. Moon, H. R. Child, W. C. Koehler, and L. J. Raubenheimer, J. Appl. Phys. **38**, 1383 (2004).
[78]Y. Li, G. Chen, W. Tong, L. Pi, J. Liu, Z. Yang, X. Wang, and Q. Zhang, Phys. Rev. Lett. **115**, 167203 (2015).